



Fault scarps and tectonic strain in young volcanic seafloor

Jie Chen^{a,b,*}, Javier Escartin^b, Mathilde Cannat^a

^a Université Paris Cité, Institut de physique du globe de Paris, CNRS, 75005 Paris, France

^b Laboratoire de Géologie, Ecole Normale Supérieure/CNRS UMR 8538, PSL Research University, Paris 75005, France

ARTICLE INFO

Editor: Carolina Lithgow-Bertelloni

Keywords:

Mid-Ocean Ridge
Autonomous Underwater Vehicle
High-resolution bathymetry
Fault scarp
Young seafloor
Tectonic strain

ABSTRACT

Fault scarps at Mid-Ocean Ridges (MOR) are recognizable on the seafloor, and often measured to estimate the tectonic component of plate divergence. This estimate, based on linear fault scarp parameters, is referred to here as apparent tectonic strain (ATS). However, ATS may differ from the actual tectonic strain at a lithosphere scale. This is clear at detachment faults at magma-poor slow-ultraslow spreading ridges that do not correspond to linear scarps yet accommodate very high strain. Here we study fault scarps in young volcanic MOR seafloor, using high-resolution (1–2 m) bathymetry data of 8 sites with spreading rates of 14–110 km/Ma. Our results show a weak correlation between ATS and factors such as spreading rate, melt flux, or thermal regime, challenging the use of ATS as a proxy for the MOR tectonic component of plate divergence. Instead, ATS is time-dependent and heterogeneous spatially, controlled by the frequency and size of dike intrusions with associated faults and volcanic eruptions that resurface the seafloor and cover faults. Our findings also have implications for estimates of tectonic extension in subaerial volcanic rifting systems that undergo similar processes.

1. Introduction

The seafloor formed at Mid-Ocean Ridges (MOR) covers >65% of the Earth's surface and is created as a response to plate divergence by the combination of magmatic accretion and tectonic extension. Magmatic accretion occurs through dike intrusions and seafloor eruptions in the upper crust and melt crystallization in the lower crust (Detrick et al., 1987; Sinton and Detrick, 1992). The tectonic component of plate divergence is taken up by slip along normal faults that develop and grow within the brittle lithosphere (Buck et al., 2005; Carbotte and Macdonald, 1994). The contribution of magmatic accretion, often denoted as the M value (Behn and Ito, 2008; Buck et al., 2005; Ito and Behn, 2008; Liu and Buck, 2020; Olive and Dublanchet, 2020), is a key parameter for MOR processes, which has predictable consequences in terms of seafloor spreading modes, axial thermal regimes, magnetic patterns, and hydrothermal circulation (Cannat et al., 2006; Chen et al., 2023; Zhou and Dymant, 2023).

As the quantification of the magmatic component of plate divergence is challenging, in practice, researchers have proposed quantifications for the apparent tectonic component (i.e., 1-M value) by summing the heaves of linear fault scarps at the seafloor and calculating the corresponding % value of total plate divergence based on the width of the study area (Bohnenstiehl and Carbotte, 2001; Carbotte and Macdonald,

1994; Chen et al., 2021; Combier et al., 2015; Cowie et al., 1994; Deschamps et al., 2007; Escartín et al., 2007, 1999; Howell et al., 2016; Le Saout et al., 2018, 2023; Olive et al., 2024). As this approach is based on measuring linear fault scarps that are apparent on the seafloor (i.e., tectonic deformation in depth is not accounted), we will refer to the resulting values as apparent tectonic strain (ATS), or apparent tectonic component of plate divergence, and examine its potential as a proxy to measure actual MOR tectonic components.

At fast-spreading ridges, plate divergence is dominated by magmatic accretion; ATS is commonly below 5% (Bohnenstiehl and Carbotte, 2001; Carbotte and Macdonald, 1994; Cowie et al., 1994; Escartín et al., 2007; Le Saout et al., 2018; Wu et al., 2023), and most near-axis faults likely form due to local stresses induced by diking (Le Saout et al., 2018; Soule et al., 2009). At slow-spreading ridges, plate divergence comprises a more significant component of tectonic extension, resulting over timescales of several hundred thousand years in the formation of axial valleys (Ito and Behn, 2008; Small, 1998). At melt-poor ridge sections, long-offset detachment faults do not produce linear scarps yet contribute between 50% to nearly 100% of the total plate divergence over long periods (MacLeod et al., 2009; Sauter et al., 2013). In contrast, volcanic seafloor at melt-rich slow and ultraslow ridge sections yields ATS values between 2 and 16% (Chen et al., 2021; Combier et al., 2015; Escartín et al., 1999; Le Saout et al., 2023), similar to or larger than those at fast

* Corresponding author.

E-mail address: chen@geologie.ens.fr (J. Chen).

ridges. The young seafloor in these volcanically active regions is a critical zone where faults nucleate and may evolve to prominent axial valley walls and off-axis abyssal hills. Yet, similar to fast ridges, faults there interact with volcanism (Chen et al., 2021; Gini et al., 2021) and mass wasting (Hughes et al., 2024) (Fig. 1a), at different temporal and spatial scales that may depend on spreading rate, resulting in ATS probably different from the actual tectonic component.

2. High-resolution bathymetry data and fault detection

Most ATS studies cited above have used shipboard bathymetry data with a resolution (20–100 m; Fig. S1a) that is insufficient to identify smaller faults. High-resolution (HR; 1–2 m) bathymetry data collected by state-of-art Autonomous Underwater Vehicle (AUV) and Remotely Operated Vehicle (ROV) revolutionizes our ability to map fine-scale volcanic and tectonic features on the seafloor (Chen et al., 2021; Le Saout et al., 2018; Wu et al., 2023).

ATS studies using such HR bathymetry data have been published for several sites at young volcanic seafloor from fast to ultraslow spreading ridges, such as the 9°N (Wu et al., 2023) (Fig. 2a) and the 16°N (Le Saout et al., 2018) of the East Pacific Ridge (EPR), the Explorer region

(Deschamps et al., 2007) (Fig. 2b) of the Juan de Fuca Ridge (JdFR), and the 50.5°E region (Chen et al., 2021) (Fig. 2h) of the Southwest Indian Ridge (SWIR). However, none of these studies proposed a global comparison. Here, we study young volcanic seafloor at 8 MOR sites over a broad range of spreading rates (14–110 km/Ma), using a compilation of available HR bathymetry data covering a total area of 400 km² (all standardized to the same distance scale and the same relative color scale in Fig. 2a–h). Estimated maximum and mean crustal ages at these sites range between ~50 and ~940 kyr, and between ~30 and ~590 kyr, respectively (Methods and Table S1 in Supplementary). The meaning of our ATS values is, therefore, different from those measured on off-axis older seafloor associated with more mature faults (Carbotte and Macdonald, 1994; Escartín et al., 1999; Howell et al., 2016; Olive et al., 2024). As a result, we identified 9188 faults and fissures in total (1833 km in length), which are used to 1) quantify ATS with a novel approach to highlight its spatial variability, 2) explore the relation between the ATS and the actual tectonic component of plate divergence, and 3) propose a conceptual synthesis of fault evolution in young volcanic seafloor over the full range of spreading rates, considering the interplay between tectonic, volcanic, and mass-wasting processes over different temporal and spatial scales.

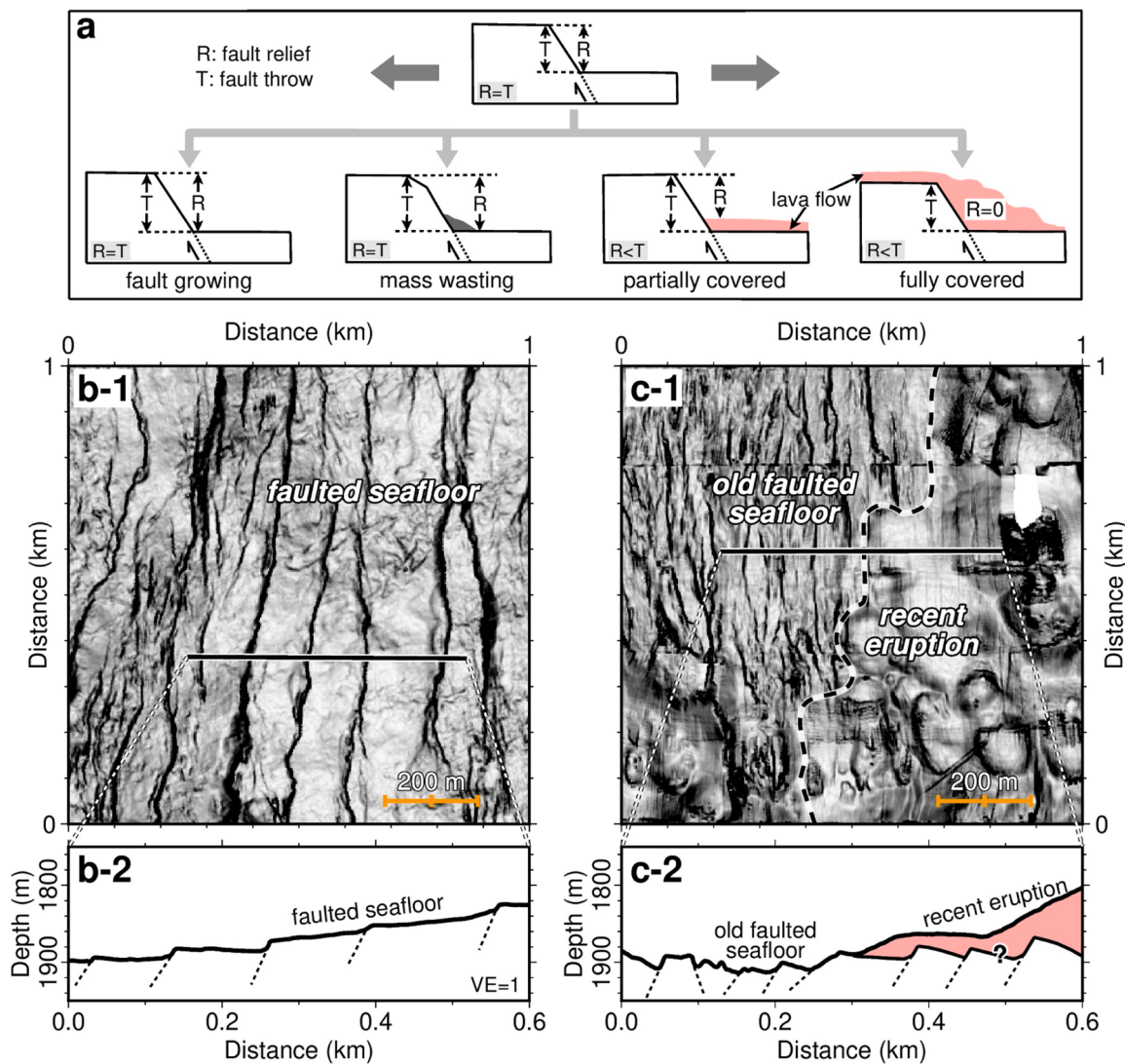


Fig. 1. Appearance of fault scarps in young volcanic seafloor. (a) Sketch of fault scarps influenced by tectonic extension, mass wasting, and lava flow. Measurements of fault relief (R) are provided, representing the minimum estimate of fault throw (T). (b-1) and (c-1) Shaded high-resolution bathymetry showing faulted seafloor and fault scarps partially covered by a recent eruption, respectively (See locations in Fig. 2g and h). Maps are in the same distance scale ($1 \times 1 \text{ km}^2$). (b-2) and (c-2) Depth profiles with no vertical exaggeration ($\text{VE}=1$).

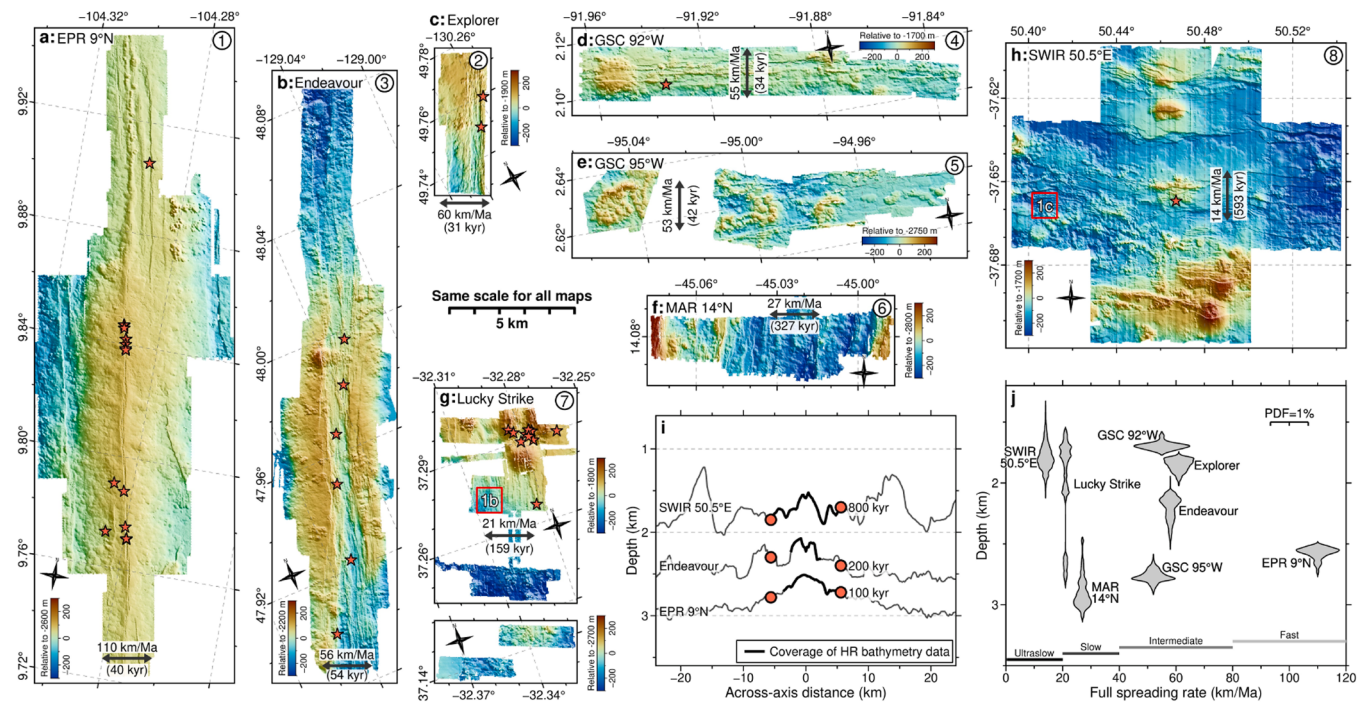


Fig. 2. High-resolution bathymetry data of 8 study sites. (a)-(h) Maps are in the same distance scale and the same relative color scale. See Fig. S2 for data locations, Fig. S3 for large-scale low-resolution shipboard bathymetric maps, and Table S1 for site information. Numerical labels (1–8) at the upper-right corner are sorted by spreading rate in descending order. Mean crustal ages (in brackets) are calculated by dividing the survey area by along-axis distance and general spreading rates (see Methods in Supplementary). Note that the Lucky Strike area (g) includes two panels from the segment center (upper) to the end (lower). Red stars indicate locations of hydrothermal vents. (i) Across-axis profiles of shipboard bathymetry data for the EPR 9°N, Endeavour, and SWIR 50.5°E study sites, showing the relationship between spatial and temporal scales. Thick black lines show the coverage of high-resolution bathymetry data. Red circles indicate different crustal ages at ~5.6 km off axis. (j) Violin plot showing the depth distribution of high-resolution bathymetry data at each site. The probability density function (PDF) is calculated with a spacing of 1 m. EPR: East Pacific Rise. GSC: Galapagos Spreading Center. MAR: Mid-Atlantic Ridge. SWIR: Southwest Indian Ridge.

3. Apparent tectonic strain

In most previous works, apparent tectonic strain (ATS) is calculated by summing the heave (based on the measurements of fault relief and dip) of ridge-parallel faults and the width of fissures, along a few selected (or regularly spaced) cross-axis transects. This approach has been applied to HR bathymetry data by researchers (Chen et al., 2021; Deschamps et al., 2007; Wu et al., 2023) in 3 of the 8 study sites considered here (i.e., EPR 9°N, Explorer, and SWIR 50.5°E; estimated ATS values in Table S1). With this approach, it is difficult to evaluate the spatial variability of ATS along and across the ridge axis. To characterize this spatial variability and ultimately link it to other processes like volcanism, we calculate the map of ATS based on the fault heave (H) and fissure width (W) over a given area. We calculate fault heave from measured fault relief (R ; Fig. 1a) along cross-axis transects spaced at $C = 2$ m (see Methods in Supplementary), applying a circular window expressed as:

$$\Sigma H = \frac{\Sigma R}{\tan(\alpha)},$$

$$ATS = 100\% \times C \cdot (\Sigma H + \Sigma W) / \pi r^2,$$

where r is the search radius of the moving circular window, ΣR , ΣH , and ΣW are accumulations of fault relief, fault heave, and fissure width within the search window, respectively, and α is the fault dip inferred here, as in previous studies (Chen et al., 2021; Deschamps et al., 2007; Le Saout et al., 2018), to have a uniform value.

To do so, we picked closed polygons of all apparent fault scarps and fissures for the 8 study sites (see Methods in Supplementary). The cumulative frequency of the maximum fault relief of each site follows an

exponential law (see log-linear plots in Fig. S4), suggesting that our picking process correctly records small fault scarps down to 2–4 m. The search radius (r) is constrained by the fault spacing measured along 2-m-spaced cross-axis transects; across the 8 study sites, the average fault spacing is 180 m, with variations among individual study sites ranging from 71 to 577 m (Table S1). The fault dip (α) is constrained by the median value of the fault dip versus fault throw stabilizing at 60–75° at throws of >50 m (Fig. S5). To evaluate the robustness of our ATS calculation, we use the combination of $r = 200$ m and $\alpha = 65^\circ$ in Figs. 3 and 4, and test other combinations of r (100 and 400 m) and α (75°) in Figs. S6–S14.

Fig. 3 shows maps of seafloor morphology, faulting pattern, and ATS of three sites with extensive coverage of HR bathymetry data (Fig. 2i): the fast-spreading EPR 9°N (110 km/Ma) with data covering the axial high (Wu et al., 2023); the intermediate-spreading Endeavour of the JdFR (56 km/Ma) with data covering the axial inflated portion (Clague et al., 2014); and the ultraslow-spreading SWIR 50.5°E (14 km/Ma) with data covering two successive constructions of inflated axial domal volcanoes (Chen et al., 2021). Based on our ATS maps, at the EPR 9°N (Fig. 3a), 85% of the young seafloor is nearly fracture-free with ATS <1% (Fig. 4a). This includes the area covered by the 2005–2006 volcanic eruption (Soule et al., 2007). ATS reaches 10% around the first pair of conjugate bounding faults (2–4 km away from the axial high summit). At the Endeavour area (Fig. 3b), faults and fissures concentrate within the graben that rifts the most inflated portion of the axis to a width of 1–2 km, resulting in local ATS values up to 20–25% (e.g., the rifted seamount near 48°N). Outside this axial graben, the seafloor is fracture-free with nearly-zero ATS. At the SWIR 50.5°E (Fig. 3c), the seafloor is extensively faulted, lacking a continuous volcanic or tectonic axis. There are three ridge-parallel fracture-free stripes (i.e., nearly-zero

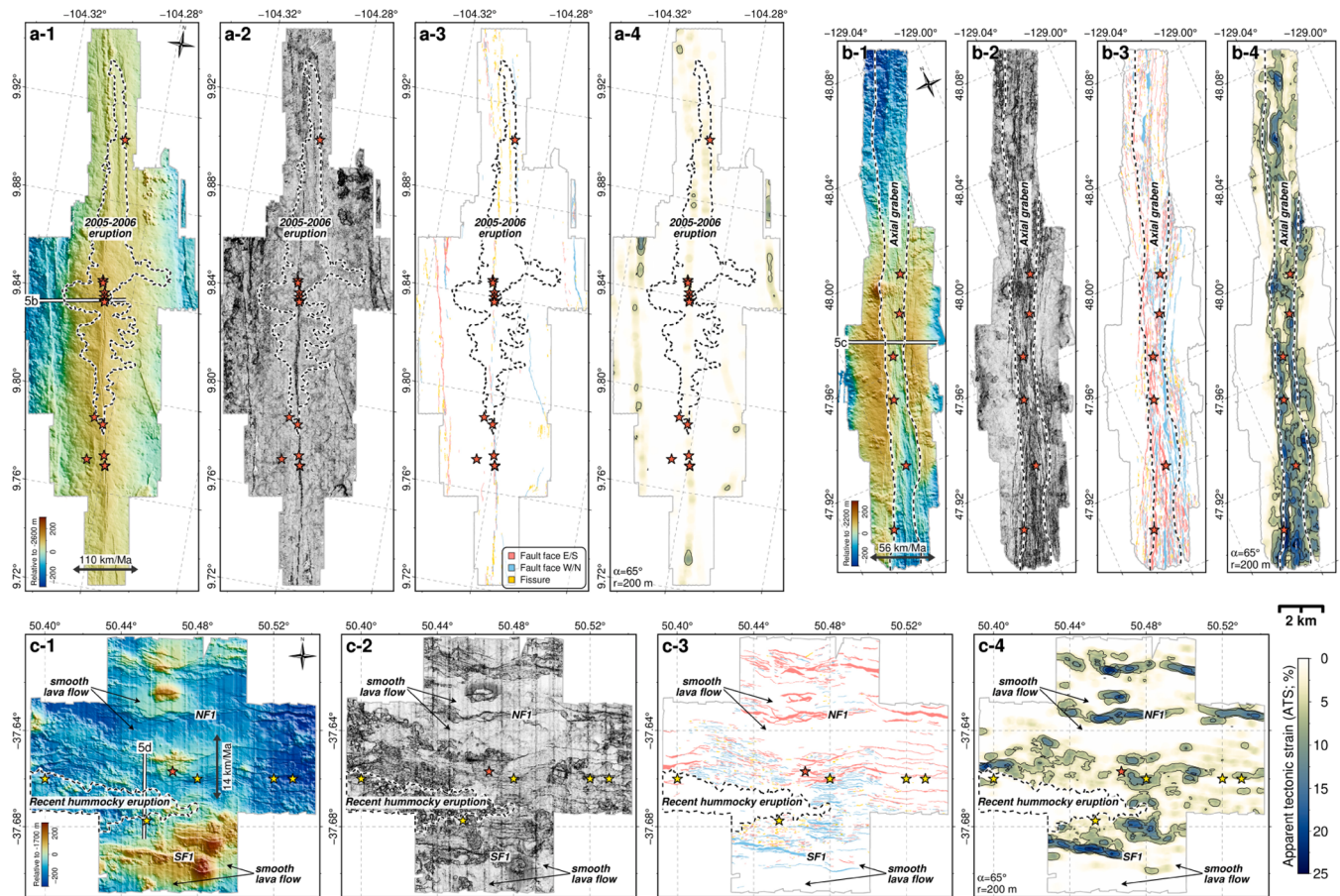


Fig. 3. Shaded maps, faulting patterns, and apparent tectonic strain maps of the EPR 9°N (a), Endeavour (b), and SWIR 50.5°E (c) study sites. All maps have the same distance scale. White solid lines are profile locations in the upper panels of Fig. 5b-d. Red stars indicate locations of hydrothermal vents. Yellow stars in (c) indicate locations of hydrothermal plume anomalies (Wu et al., 2022; Yue et al., 2019). Dashed lines represent the extent of the 2005–2006 eruption (a) (Soule et al., 2007), the axial graben (b), and the recent hummocky lava flows built by multiple eruptions (c) (Chen et al., 2021). NF1 and SF1 in (c) are conjugate northern and southern bounding faults, respectively (Chen et al., 2021). (a-2), (b-2), and (c-2) Shaded high-resolution bathymetry maps. (a-3), (b-3), and (c-3) Interpreted faults and fissures. Red areas are faults facing east or south. Blue areas are faults facing west or north. Orange areas are fissures. (a-4), (b-4), and (c-4) Calculated apparent tectonic strain (ATS) based on interpreted faults and fissures. Color scale is the same for the three sites. Fault dip and search radius are given as $\alpha = 65^\circ$ and $r = 200$ m in the ATS calculation. Other combinations of α (75°) and r (100 and 400 m) of these three sites can be found in Figs. S6–S8.

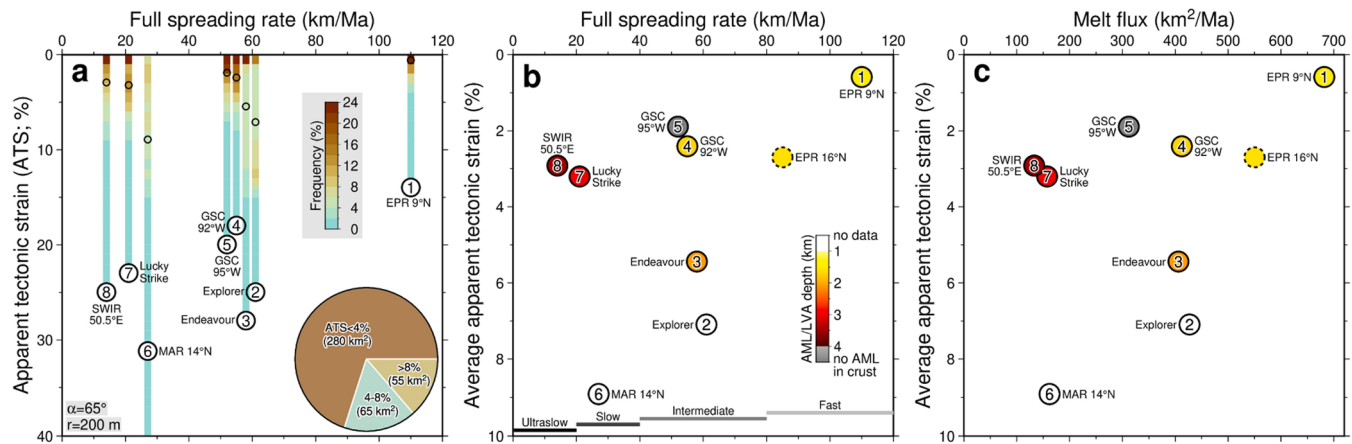


Fig. 4. Apparent tectonic strain estimated using high-resolution bathymetry data. (a) Range and frequency of apparent tectonic strain (ATS) of 8 study sites plotted vs. spreading rate. Vertical bars show the ATS range, and the frequency is color-coded. Small open circles mark the average ATS, also shown in (b) and (c). Fault dip and search radius are given as $\alpha = 65^\circ$ and $r = 200$ m in the ATS calculation (see Fig. S14 for other combinations of α and r). Pie chart shows the proportion of the mapped seafloor (400 km² in total) at the ATS of <4%, 4–8%, and >8%. (b) Average ATS is calculated using all faults and fissures within the mapped area, except for the EPR 16°N, where average ATS is calculated by averaging ATS along five cross-axis sections (Le Saout et al., 2018). AML/LVA depth is color-coded, and see Table S1 for the compilation (Chen et al., 2023). AML: axial melt lens. LVA: low-velocity anomaly. (c) Average ATS plotted vs. melt flux. Melt flux is the product of spreading rate and magmatic crustal thickness (Table S1).

ATS): the smooth lava flow surrounding the northern bounding fault system (NF1), the recent hummocky lava flows built by multiple eruptions, and the smooth lava flow region in the southernmost part of the mapped area (Chen et al., 2021). Between these fracture-free stripes, ATS reaches up to >20%.

The other five study sites (see Figs. S9–S13) include the Explorer area (60 km/Ma) of the JdFR, similar to the Endeavour area, that has concentrated faulting within the axial graben with ATS of up to 24% (Fig. S9). At the 92°W (55 km/Ma) and 95°W (53 km/Ma) regions of the intermediate-spreading Galapagos Spreading Center (GSC), with data covering the axial high and the bottom of the axial valley, respectively, local ATS values vary between 0 and 18% (Figs. S10 and S11). At the 14°N (27 km/Ma) region of slow-spreading Mid-Atlantic Ridge (MAR), data covers the entire 9-km-wide axial valley, and local ATS values vary between >40% near the valley wall and nearly-zero in the youngest seafloor (Fig. S12). At the Lucky Strike area (21 km/Ma) of the MAR, local ATS values peak over the inflated domal volcano at the segment center (>20%) and decrease toward the segment end (<1%) (Fig. S13). We also compare with a fault study at the EPR 16°N (85 km/Ma) using HR (1 m) bathymetry data, which illustrates an along-axis variation of ATS between 1.4 and 6.4% assuming a uniform fault dip of 65°, measured along five cross-axis transects spaced at 2 km (Le Saout et al., 2018).

Therefore, there are large variations of ATS within each study site at local spatial scales. To convey this local variability in faulting, and in the associated ATS values, Fig. 4a shows both the range and the frequency distribution of ATS for the 8 study sites. Overall, most of the mapped seafloor (280 km² out of the total 400 km²) displays ATS of <4%, and only a small portion of the seafloor (55 km²) exhibits ATS exceeding 8%. These values are nearly independent of the given search radius (Fig. S14a and b).

4. Fault scarps in young seafloor poorly reflect the tectonic component of plate divergence

It is widely hypothesized that the tectonic component of plate divergence decreases with the increases in spreading rate and melt flux (the product of spreading rate and magmatic crustal thickness) (Behn and Ito, 2008; Olive and Dublanchet, 2020; Shaw and Lin, 1996). We integrate our observations and previous geophysical studies at the 8 study sites, together with the EPR 16°N where apparent tectonic strain (ATS) averages 2.7% based on five cross-axis transects (Le Saout et al., 2018). The average ATS of the 8 study sites (calculated using all faults and fissures within the mapped area) is lowest at the fastest-spreading, highest-melt-flux study site (EPR 9°N), but others show no clear correlation with spreading rate and inferred melt flux (Fig. 4b and c and data listed in Table S1). There is, however, a broader range of both the average ATS values and the local ATS variability for study sites at intermediate to slow spreading rates and melt fluxes (Fig. 4). At the scale of a given study area, the relation between ATS and melt flux may even be opposite to predictions: for example, the inflated domal volcano in the center of the Lucky Strike area, where the local melt flux is highest, displays the highest local ATS (Fig. S13c), possibly reflecting the variations from localized deformation at a narrow graben within the rift valley, to distributed deformation throughout the full width of the rift valley floor, from the center to the end of the Lucky Strike segment.

This overall lack of a correlation, or in some cases correlations that go against common expectations, means that parameters beyond spreading rate and melt flux also affect ATS values. The depth of the axial melt lens (AML), when present, may be one such parameter because it represents a lower bound for the thickness of the axial lithosphere and, therefore, could be expected to correlate with axial faulting characteristics. However, we show that AML depth is not correlated either with ATS values (Fig. 4b). AML depths are similar at EPR 9°N and 16°N (~1.5 km below the seafloor; (Carbotte et al., 1998; Marjanović et al., 2014), yet the average ATS at the EPR 16°N (Le Saout et al., 2018)

is >4 times higher than that of the EPR 9°N (2.7% vs. 0.59%; Fig. 4b). At the intermediate-spreading GSC, the 92°W area has a higher melt flux and a shallow AML (1.4 km), while the 95°W area does not have a crustal AML (Blacic et al., 2004), yet their average ATS values are close (~2%; Fig. 4b and c). At the intermediate-spreading JdFR, the Endeavour area has a 2.1-km deep AML (Arnoux et al., 2019; Carbotte et al., 2006) and an average ATS value of 5.4% (Fig. 4b) that is ~1.8 times higher than that of the slow- and ultraslow-spreading Lucky Strike and SWIR 50.5°E areas where the AML and/or seismic low-velocity anomaly (LVA) are significantly deeper (3–4 km) (Li et al., 2015; Singh et al., 2006).

These comparisons demonstrate that fault scarps in young volcanic seafloor do not accurately reflect the long-term, lithospheric-scale tectonic component of plate divergence. ATS values are, therefore, not appropriate for estimating the M value at any MOR locations. The hypothesis we make here is that faulting characteristics and the resulting ATS values are also strongly affected by two types of volcanic processes. The first volcanic process reduces ATS values and is simply that lava flows may bury pre-existing fault scarps. This is typically the case with high-effusion-rate smooth lava flows that have been documented to cover the seafloor up to 2 km from the eruptive source (Chen et al., 2021; Soule et al., 2007). At the EPR 9°N, fault scarps in young seafloor are presumably buried by lavas from eruptions that occurred as recently as 2005–2006 (Escartín et al., 2007; Soule et al., 2007); while at slow-spreading centers, these scarps may steer flows that partially cover these scarps (Gini et al., 2021). At the SWIR 50.5°E area, several eruptions of smooth lava flow that occurred over the past 780 kyrs also lead to fracture-free stripes (Chen et al., 2021) (Fig. 3c). The second volcanic process increases ATS values and involves the formation of linear normal fault scarps in response to dikes stalling at depth and not reaching to the seafloor (Chadwick and Embley, 1998; Rubin, 1992). At the EPR 9°N and 16°N, it has been proposed that most faults in the axial summit trough region originate that way (Le Saout et al., 2018; Soule et al., 2009). Locally high ATS values in volcanically-robust portions of intermediate-slow-ultraslow ridges (i.e., the Endeavour, Explorer, Lucky Strike, and SWIR 50.5°E study areas) could also be explained by frequent dike intrusions, if a significant proportion does not result in eruptions (Gudmundsson and Brenner, 2004; Hooft et al., 1996).

In Fig. S15, we also estimate the average ATS rates of the 8 study sites and the EPR 16°N by dividing the average ATS values by mean crustal ages, yielding a range from 3×10^{-8} to 2.5×10^{-6} yr⁻¹. However, uncertainties must be considered in these estimates, particularly those related to the inherited use of general and uniform spreading rates in axial regions (see Methods in Supplementary), which is beyond the scope of this paper that focuses on small-scale temporal and spatial variability of faulting.

5. A synthesis of fault evolution in young seafloor

Fault scarps across all spreading rates should grow over time if evolving only in response to tectonic extension. The high temporal and spatial variability in apparent tectonic strain (ATS) is therefore interpreted here as primarily related to volcanic eruptions and/or dike injections (Fig. 5a). In young volcanic seafloor, a high apparent tectonic strain could result from a high tectonic component of plate divergence (i.e., a low M value) and/or a high frequency of dike injections, combined with an overall low eruption rate. However, we do not deal with detachment faults at magma-poor slow-ultraslow spreading ridges that accommodate very high strain (up to 50–100%).

We, therefore, should be cautious when comparing the temporal and spatial variability of ATS at different spreading rates and melt fluxes, for example, between the EPR 9°N, the Endeavour, and the SWIR 50.5°E study sites (spreading rates of 110, 56, and 14 km/Ma, respectively; Fig. 5b–d). At a given area, the seafloor at the SWIR 50.5°E records a history that is about 8 and 4 times longer than that of the EPR 9°N and the Endeavour, respectively. The interval of volcanic eruptions at the EPR 9°N is only tens of years (Perfit and Chadwick, 1998; Soule et al.,

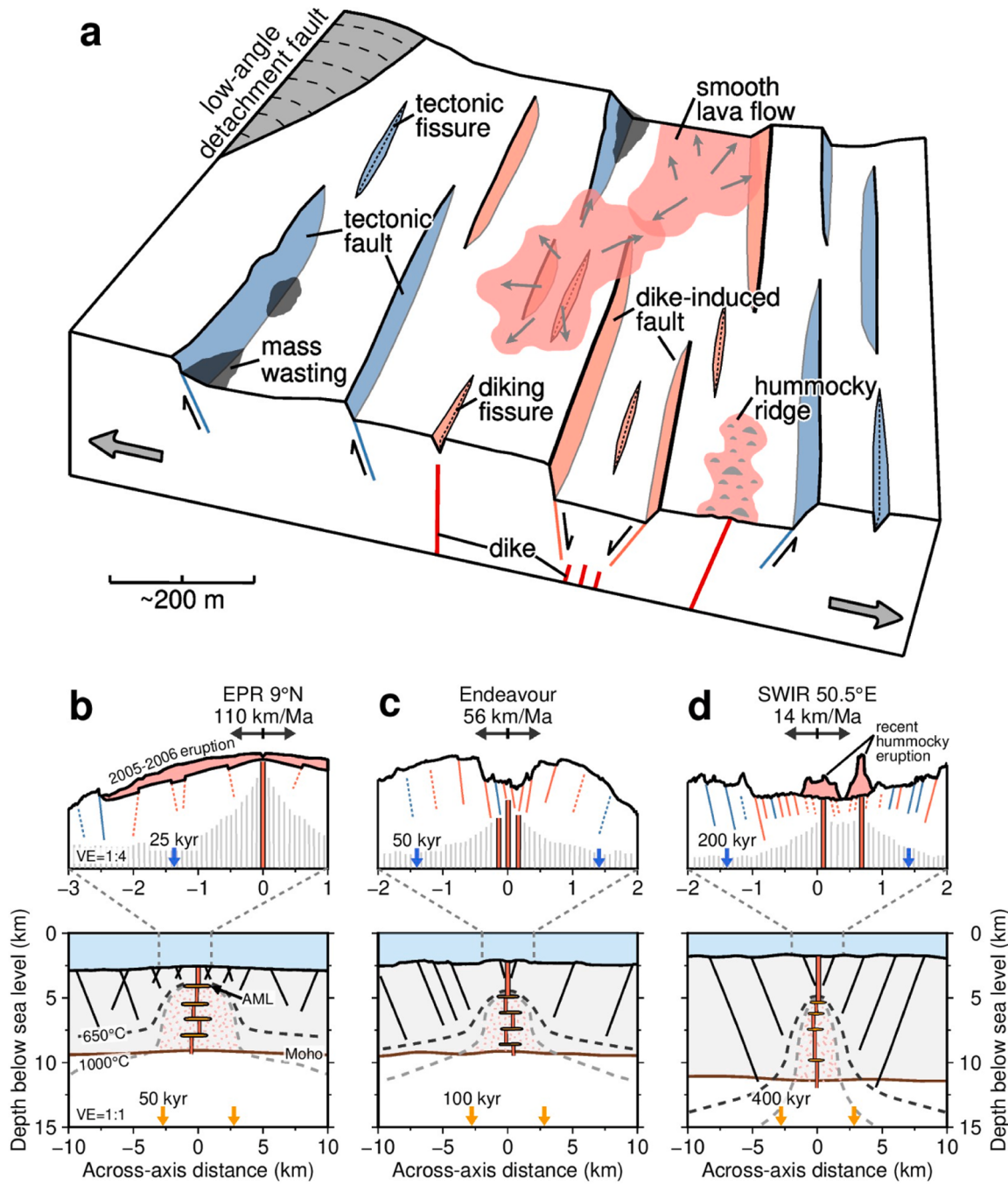


Fig. 5. Fault synthesis in young seafloor. (a) Sketch of the fault synthesis. Fault scarps and fissures can be induced by tectonic stretching (blue area) and dike intrusions (pink area) or covered by volcanic eruptions and mass wasting. A low-angle detachment fault is also drawn, although our data do not map it. (b)-(d) Upper panels ($VE=1:4$) are based on high-resolution bathymetric profiles of the fast-spreading EPR 9°N, the intermediate-spreading Endeavour, and the ultraslow-spreading SWIR 50.5°E (see profile locations in Fig. 3). Blue arrows indicate different crustal ages at ~1.4 km off axis. Vertical red and gray bars indicate active and inactive dikes, respectively. Blue and pink lines represent faults induced by tectonic stretching and dike intrusions, respectively. Dashed lines represent faults covered by lava flows. Lower panels ($VE=1:1$) of crustal cross-sections are constrained by seismic studies of the EPR 9°N (Detrick et al., 1987; Dunn et al., 2000; Marjanović et al., 2014), the Endeavour (Arnoux et al., 2019; Carbotte et al., 2006), and the SWIR 50.5°E (Li et al., 2015). Orange arrows indicate different crustal ages at ~2.8 km off axis. Solid black lines indicate faults. The 650 °C (dashed black lines) and 1000 °C (dashed gray lines) isotherms represent the base of the brittle lithosphere and the basaltic solidus, respectively. AML: axial melt lens.

2007). It is probably 1 to 3 orders of magnitude higher for the Endeavour and the SWIR 50.5°E (Perfit and Chadwick, 1998). The seafloor at the EPR 9°N is, therefore, more frequently resurfaced by lava flows. Eruptions are also discrete events in time and space, and the spatial extent of volcanic eruptions is mainly influenced by lava effusion rates (Chen et al., 2021). A high lava-effusion-rate eruption produces extensive lava flows efficiently covering seafloor (e.g., the 2005–2006 eruption at the

EPR 9°N in Fig. 5b), and a low lava-effusion-rate eruption produces patchy hummocky cones/ridges covering seafloor around the eruptive source (e.g., the recent hummocky eruption at the SWIR 50.5°E in Fig. 5d). In all cases, lava-buried faults may be reactivated by subsequent tectonic or dike-induced deformation.

Dike-induced faults can also vary temporally and spatially, influenced by factors such as the axial thermal regime, the frequency of dike

injections, and the length and depth of intrusion. At fast spreading ridges, a shallow magma chamber (~1.5 km below the seafloor) is an ideal setting to develop dike-induced faults, as the brittle lid is relatively weak and thin. For example, at the EPR 9°N, this setting leads to the development of the axial summit trough and the nucleation of asymmetric faults outside the trough (Marjanović et al., 2024; Soule et al., 2009); faults can be induced by the formation of new AMLs, while melt may be transported into existing faults to trigger eruptions, resulting in a fluctuating rate of apparent fault growth over short timescales. As dike-induced faults typically form symmetrically about the dike (Chadwick and Embley, 1998; Rubin, 1992), continuous high-frequency dike intrusions with a low proportion of associated eruptions would limit resurfacing but facilitate the development of the axial graben, such as at the Endeavour area (Fig. 5c). As the new seafloor moves away from active axial volcanic systems, faults may grow responding to far-field tectonic stretching, e.g., the paired valley-wall faults in the MAR 14°N area (Figs. 2f and S12) that are typical of volcanic slow-ultraslow spreading ridges.

Furthermore, our interpretation of the faulting patterns and ATS values in young volcanic seafloor, summarized in Fig. 5a, may be applicable to subaerial volcanic centers. For example, the East African rift system and the Iceland volcanic system display significant along-rift variations in faulting patterns and ATS (Corti et al., 2021; Dumont et al., 2019; Siegburg et al., 2020), attributable to this spatial variability in tectonic and volcanic interactions. Similarly, volcanic centers there often correspond to a relatively high ATS, coinciding with recent feeder dikes (Acocella and Tripanera, 2016; Dumont et al., 2019; Grandin et al., 2010). Volcanic deposits can also fully or partially cover fault scarps (Siegburg et al., 2020), thus lowering the apparent fault offset and hence, the ATS, as we observe at mid-ocean ridges.

CRediT authorship contribution statement

Jie Chen: Writing – review & editing, Writing – original draft, Visualization, Validation, Resources, Methodology, Formal analysis, Data curation, Conceptualization. **Javier Escartín:** Writing – review & editing, Validation, Methodology, Conceptualization. **Mathilde Cannat:** Writing – review & editing, Validation, Funding acquisition, Conceptualization.

Declaration of competing interest

The authors declare that they have no known competing financial interests or personal relationships that could have appeared to influence the work reported in this paper.

Acknowledgments

This work was supported by ANR project “Ridge Factory Slow” (ANR-18-CE01-000201). Jie Chen was funded by Naturalia & Biologia. This paper also benefitted from constructive reviews by Jeff Karson and an anonymous reviewer. Figures are generated using GMT-6 (<http://www.generic-mapping-tools.org/>). This is IPGP contribution #4282.

Supplementary materials

Supplementary material associated with this article can be found, in the online version, at [doi:10.1016/j.epsl.2024.119174](https://doi.org/10.1016/j.epsl.2024.119174).

Data availability

Bathymetry data can be found in the following links: EPR9°N (<https://doi.org/10.26022/IEDA/330373>), Endeavour (<https://doi.org/10.1594/IEDA/321996>), GSC 92°W and 95°W (<https://doi.org/10.1594/IEDA/318210>), MAR 14°N (<https://doi.org/10.26022/IEDA/330198>), Lucky Strike (<https://doi.org/10.17882/80574>), and SWIR 50.5°E (<https://doi.org/10.5281/zenodo.5147241>). All digital faults and fissures, a screen record showing the picking process of faults and fissures, and calculated grid files of apparent tectonic strain of all sites can be found in <https://doi.org/10.6084/m9.figshare.25757730>.

References

- Acocella, V., Tripanera, D., 2016. How diking affects the tectonomagmatic evolution of slow spreading plate boundaries: overview and model. *Geosphere* 12, 867–883. <https://doi.org/10.1130/GES01271.1>.
- Arnoux, G.M., Toomey, D.R., Hoot, E.E., Wilcock, W.S.D., 2019. Seismic imaging and physical properties of the Endeavour segment: evidence that skew between mantle and crustal magmatic systems governs spreading center processes. *Geochem. Geophys. Geosyst.* 20, 1319–1339. <https://doi.org/10.1029/2018GC007978>.
- Behn, M.D., Ito, G., 2008. Magmatic and tectonic extension at mid-ocean ridges: 1. Controls on fault characteristics. *Geochem. Geophys. Geosyst.* 9, 8–10. <https://doi.org/10.1029/2008GC001965>.
- Blacic, T.M., Ito, G., Canales, J.P., Detrick, R.S., Sinton, J., 2004. Constructing the crust along the Galapagos Spreading Center 91.3°–95.5°W: correlation of seismic layer 2A with axial magma lens and topographic characteristics. *J. Geophys. Res. Solid Earth* 109, B10310. <https://doi.org/10.1029/2004JB003066>.
- Bohnenstiehl, D.W.R., Carbotte, S.M., 2001. Faulting patterns near 19°30'S on the East Pacific rise: fault formation and growth at a superfast spreading center. *Geochem. Geophys. Geosyst.* 2, 1056. <https://doi.org/10.1029/2001GC000156>.
- Buck, W.R., Lavier, L.L., Poliakov, A.N.B., 2005. Modes of faulting at mid-ocean ridges. *Nature* 434, 719–723. <https://doi.org/10.1038/nature03358>.
- Cannat, M., Sauter, D., Mendel, V., Ruellan, E., Okino, K., Escartín, J., Combier, V., Baala, M., 2006. Modes of seafloor generation at a melt-poor ultraslow-spreading ridge. *Geology* 34, 605–608. <https://doi.org/10.1130/G22486.1>.
- Carbotte, S., Mutter, C., Mutter, J., Ponce-Correa, G., 1998. Influence of magma supply and spreading rate on crustal magma bodies and emplacement of the extrusive layer: insights from the East Pacific Rise at lat 16°N. *Geology* 26, 455–458. [https://doi.org/10.1130/0091-7613\(1998\)026<0455:OMSA>2.3.CO;2](https://doi.org/10.1130/0091-7613(1998)026<0455:OMSA>2.3.CO;2).
- Carbotte, S.M., Nedimovic, M., Diebold, J., 2006. Rift topography linked to magmatism at the intermediate spreading Juan de Fuca Ridge. *Geology* 34, 209–212. <https://doi.org/10.1130/G21969.1>.
- Carbotte, S.M., Macdonald, K.C., 1994. Comparison of seafloor tectonic fabric at intermediate, fast, and super fast spreading ridges: influence of spreading rate, plate motions, and ridge segmentation on fault patterns. *J. Geophys. Res. Solid Earth* 99, 13609–13631. <https://doi.org/10.1029/93jb02971>.
- Chadwick, W.W., Embley, R.W., 1998. Graben formation associated with recent dike intrusions and volcanic eruptions on the mid-ocean ridge. *J. Geophys. Res. Solid Earth* 103, 9807–9825. <https://doi.org/10.1029/97jb02485>.
- Chen, J., Cannat, M., Tao, C., Sauter, D., Munschy, M., 2021. 780 thousand years of upper-crustal construction at a melt-rich segment of the ultraslow spreading Southwest Indian Ridge 50°28'E. *J. Geophys. Res. Solid Earth* 126, e2021JB022152. <https://doi.org/10.1029/2021JB022152>.
- Chen, J., Olive, J.A., Cannat, M., 2023. Beyond spreading rate: controls on the thermal regime of mid-ocean ridges. In: Proc. Natl. Acad. Sci. 120, e2306466120. <https://doi.org/10.1073/pnas.2306466120>.
- Clague, D.A., Dreyer, B.M., Paduan, J.B., Martin, J.F., Caress, D.W., Gill, J.B., Kelley, D.S., Thomas, H., Portner, R.A., Delaney, J.R., Guilderston, T.P., McGann, M.L., 2014. Eruptive and tectonic history of the Endeavour Segment, Juan de Fuca Ridge, based on AUV mapping data and lava flow ages. *Geochem. Geophys. Geosyst.* 15, 3364–3391. <https://doi.org/10.1002/2014GC005415>.
- Combier, V., Seher, T., Singh, S.C., Crawford, W.C., Cannat, M., Escartín, J., Dusunur, D., 2015. Three-dimensional geometry of axial magma chamber roof and faults at Lucky Strike volcano on the Mid-Atlantic Ridge. *J. Geophys. Res. Solid Earth* 120, 5379–5400. <https://doi.org/10.1002/2015JB012365>.
- Corti, N., Bonali, F.L., Mariotti, F.P., Tibaldi, A., Russo, E., Hjartardóttir, Á.R., Einarsson, P., Rigoni, V., Bressan, S., 2021. Fracture kinematics and holocene stress field at the Krafla rift, northern Iceland. *Geosci* 11, 1–27. <https://doi.org/10.3390/geosciences11020101>.
- Cowie, P.A., Malinverno, A., Ryan, W.B.F., Edwards, M.H., 1994. Quantitative fault studies on the East Pacific Rise: a comparison of sonar imaging techniques. *J. Geophys. Res.* 99, 15205. <https://doi.org/10.1029/94jb00041>.
- Deschamps, A., Tivey, M., Embley, R.W., Chadwick, W.W., 2007. Quantitative study of the deformation at Southern Explorer Ridge using high-resolution bathymetric data. *Earth Planet. Sci. Lett.* 259, 1–17. <https://doi.org/10.1016/j.epsl.2007.04.007>.
- Detrick, R.S., Buhl, P., Vera, E., Mutter, J., Orcutt, J., Madsen, J., Brocher, T., 1987. Multi-channel seismic imaging of a crustal magma chamber along the East Pacific Rise. *Nature* 326, 35–41. <https://doi.org/10.1038/326035a0>.
- Dumont, S., Klinger, Y., Socquet, A., Escartín, J., Grandin, R., Jacques, E., Medynski, S., Doubre, C., 2019. Rifting processes at a continent-ocean transition rift revealed by fault analysis: example of Dabbahu-Manda-Hararo Rift (Ethiopia). *Tectonics* 38, 190–214. <https://doi.org/10.1029/2018TC005141>.
- Dunn, R.A., Toomey, D.R., Solomon, S.C., 2000. Three-dimensional seismic structure and physical properties of the crust and shallow mantle beneath the East Pacific Rise at 9°30'N. *J. Geophys. Res. Solid Earth* 105, 23537–23555. <https://doi.org/10.1029/2000jb900210>.

- Escartín, J., Cowie, P.A., Searle, R.C., Allerton, S., Mitchell, N.C., MacLeod, C.J., Slootweg, A.P., 1999. Quantifying tectonic strain and magmatic accretion at a slow spreading ridge segment, Mid-Atlantic Ridge, 29°N. *J. Geophys. Res. Solid Earth* 104, 10421–10437. <https://doi.org/10.1029/1998jb900097>.
- Escartín, J., Soule, S.A., Fornari, D.J., Tivey, M.A., Schouten, H., Perfit, M.R., 2007. Interplay between faults and lava flows in construction of the upper oceanic crust: the East Pacific Rise crest 9°25'–9°58'N. *Geochem. Geophys. Geosyst.* 8, Q06005. <https://doi.org/10.1029/2006GC001399>.
- Gini, C., Escartín, J., Cannat, M., Barreyre, T., 2021. Extrusive upper crust formation at slow-spreading ridges: fault steering of lava flows. *Earth Planet. Sci. Lett.* 576, 117202. <https://doi.org/10.1016/j.epsl.2021.117202>.
- Grandin, R., Socquet, A., Doin, M.P., Jacques, E., De Chabalier, J.B., King, G.C.P., 2010. Transient rift opening in response to multiple dike injections in the Manda Hararo rift (Afar, Ethiopia) imaged by time-dependent elastic inversion of interferometric synthetic aperture radar data. *J. Geophys. Res. Solid Earth* 115, B09403. <https://doi.org/10.1029/2009JB006883>.
- Gudmundsson, A., Brenner, S.L., 2004. Local stresses, dyke arrest and surface deformation in volcanic edifices and rift zones. *Ann. Geophys.* 47, 1433–1454. <https://doi.org/10.4401/ag-3352>.
- Hooft, E.E.E., Schouten, H., Detrick, R.S., 1996. Constraining crustal emplacement processes from the variation in seismic layer 2A thickness at the East Pacific Rise. *Earth Planet. Sci. Lett.* 142, 289–309. [https://doi.org/10.1016/0012-821x\(96\)00101-x](https://doi.org/10.1016/0012-821x(96)00101-x).
- Howell, S.M., Ito, G., Behn, M.D., Martinez, F., Olive, J.-A., Escartín, J., 2016. Magmatic and tectonic extension at the Chile Ridge: evidence for mantle controls on ridge segmentation. *Geochem. Geophys. Geosyst.* 17, 2354–2373. <https://doi.org/10.1002/2016GC006380>.
- Hughes, A., Olive, J.-A., Malatesta, L.C., Escartín, J., 2024. Characterization of bedrock mass-wasting at fault-bound abyssal hills. *Earth Planet. Sci. Lett.* 648, 119073. <https://doi.org/10.1016/j.epsl.2024.119073>.
- Ito, G., Behn, M.D., 2008. Magmatic and tectonic extension at mid-ocean ridges: 2. Origin of axial morphology. *Geochem. Geophys. Geosyst.* 9, 9–12. <https://doi.org/10.1029/2008GC001970>.
- Le Saout, M., Palgan, D., Devey, C.W., Lux, T.S., Petersen, S., Thorhallsson, D., Tomkowicz, A., Brix, S., 2023. Variations in volcanism and tectonics along the hotspot-influenced Reykjanes ridge. *Geochem. Geophys. Geosyst.* 24, e2022GC010788. <https://doi.org/10.1029/2022GC010788>.
- Le Saout, M., Thibaud, R., Gente, P., 2018. Detailed analysis of near tectonic features along the East Pacific rise at 16°N, near the mathematician hot spot. *J. Geophys. Res. Solid Earth* 123, 4478–4499. <https://doi.org/10.1029/2017JB015301>.
- Li, J., Jian, H., Chen, Y.J., Singh, S.C., Ruan, A., Qiu, X., Zhao, M., Wang, X., Niu, X., Ni, J., Zhang, J., 2015. Seismic observation of an extremely magmatic accretion at the ultraslow spreading Southwest Indian Ridge. *Geophys. Res. Lett.* 42, 2656–2663. <https://doi.org/10.1002/2014GL062521>.
- Liu, Z., Buck, W.R., 2020. Global trends of axial relief and faulting at plate spreading centers imply discrete magmatic events. *J. Geophys. Res. Solid Earth* 125, e2020JB019465. <https://doi.org/10.1029/2020JB019465>.
- MacLeod, C.J., Searle, R.C., Murton, B.J., Casey, J.F., Mallows, C., Unsworth, S.C., Achenbach, K.L., Harris, M., 2009. Life cycle of oceanic core complexes. *Earth Planet. Sci. Lett.* 287, 333–344. <https://doi.org/10.1016/j.epsl.2009.08.016>.
- Marjanović, M., Carbotte, S.M., Carton, H., Nedimović, M.R., Mutter, J.C., Canales, J.P., 2014. A multi-sill magma plumbing system beneath the axis of the East Pacific Rise. *Nat. Geosci.* 7, 825–829. <https://doi.org/10.1038/ngeo2272>.
- Marjanović, M., Chen, J., Escartín, J., Parnell-Turner, R., Wu, J.-N., 2024. Magmatic-induced tectonics at the East Pacific Rise 9°50'N: evidence from high-resolution characterization of seafloor and subseafloor. In: *Proc. Natl. Acad. Sci.* 121, e2401440121. <https://doi.org/10.1073/pnas.2401440121>.
- Olive, J.A., Dublanchet, P., 2020. Controls on the magmatic fraction of extension at mid-ocean ridges. *Earth Planet. Sci. Lett.* 549, 116541. <https://doi.org/10.1016/j.epsl.2020.116541>.
- Olive, J.A., Ekström, G., Buck, W.R., Liu, Z., Escartín, J., Bickert, M., 2024. Mid-ocean ridge unfaulting revealed by magmatic intrusions. *Nature* 628, 782–787. <https://doi.org/10.1038/s41586-024-07247-w>.
- Perfit, M.R., Chadwick, W.W., 1998. Magmatism at mid-ocean ridges: constraints from volcanological and geochemical investigations. *Geophys. Monogr. Ser.* 106, 59–115. <https://doi.org/10.1029/GM106p0059>.
- Rubin, A.M., 1992. Dike-induced faulting and graben subsidence in volcanic rift zones. *J. Geophys. Res.* 97, 1839–1858. <https://doi.org/10.1029/91JB02170>.
- Sauter, D., Cannat, M., Rouméon, S., Andreani, M., Birot, D., Bronner, A., Brunelli, D., Carlut, J., Delacour, A., Guyader, V., MacLeod, C.J., Manatschal, G., Mendel, V., Ménez, B., Pasini, V., Ruellan, E., Searle, R., 2013. Continuous exhumation of mantle-derived rocks at the Southwest Indian Ridge for 11 million years. *Nat. Geosci.* 6, 314–320. <https://doi.org/10.1038/ngeo1771>.
- Shaw, W.J., Lin, J., 1996. Models of ocean ridge lithospheric deformation: dependence on crustal thickness, spreading rate, and segmentation. *J. Geophys. Res. Solid Earth* 101, 17977–17993. <https://doi.org/10.1029/96jb00949>.
- Siegburg, M., Bull, J.M., Nixon, C.W., Keir, D., Geron, T.M., Corti, G., Abebe, B., Sanderson, D.J., Ayele, A., 2020. Quantitative constraints on faulting and fault slip rates in the northern main Ethiopian rift. *Tectonics* 39, e2019TC006046. <https://doi.org/10.1029/2019TC006046>.
- Singh, S.C., Crawford, W.C., Carton, H., Seher, T., Combier, V., Cannat, M., Canales, J.P., Düsünür, D., Escartín, J., Miranda, J.M., 2006. Discovery of a magma chamber and faults beneath a Mid-Atlantic Ridge hydrothermal field. *Nature* 442, 1029–1032. <https://doi.org/10.1038/nature05105>.
- Sinton, J.M., Detrick, R.S., 1992. Mid-ocean ridge magma chambers. *J. Geophys. Res.* 97, 197–216. <https://doi.org/10.1029/91JB02508>.
- Small, C., 1998. Global systematics of mid-ocean ridge morphology. *Geophys. Monogr. Ser.* 1–25. <https://doi.org/10.1029/GM106p0001>.
- Soule, S.A., Escartín, J., Fornari, D.J., 2009. A record of eruption and intrusion at a fast spreading ridge axis: axial summit trough of the East Pacific Rise at 9°10'N. *Geochem. Geophys. Geosyst.* 10, Q10T07. <https://doi.org/10.1029/2008GC002354>.
- Soule, S.A., Fornari, D.J., Perfit, M.R., Rubin, K.H., 2007. New insights into mid-ocean ridge volcanic processes from the 2005–2006 eruption of the East Pacific Rise, 9°46'N–9°56'N. *Geology* 35, 1079–1082. <https://doi.org/10.1130/G23924A.1>.
- Wu, J.N., Parnell-Turner, R., Fornari, D.J., Berrios-Rivera, N., Barreyre, T., McDermott, J. M., 2023. The role of on- and off-axis faults and fissures during eruption cycles and crustal accretion at 9°50'N, East Pacific rise. *Geochem. Geophys. Geosyst.* 24, e2022GC010794. <https://doi.org/10.1029/2022GC010794>.
- Wu, T., Tao, C., Zhang, J., Zhang, G., Zhou, J., Bin, S., 2022. Near-bottom survey of hydrothermal sulfide on an extremely magmatic accretion segment along an ultraslow-spreading ridge. *Deep. Res. Part I Oceanogr. Res. Pap.* 187, 103830. <https://doi.org/10.1016/j.dsr.2022.103830>.
- Yue, X., Li, H., Ren, J., Tao, C., Zhou, J., Wang, Y., Lü, X., 2019. Seafloor hydrothermal activity along mid-ocean ridge with strong melt supply: study from segment 27, southwest Indian ridge. *Sci. Rep.* 9, 9874. <https://doi.org/10.1038/s41598-019-46299-1>.
- Zhou, F., Dymant, J., 2023. Temporal and spatial variation of seafloor spreading at ultraslow spreading ridges: contribution of marine magnetics. *Earth Planet. Sci. Lett.* 602, 117957. <https://doi.org/10.1016/j.epsl.2022.117957>.